Chemical Engineering Journal 526 (2025) 171028

Contents lists available at ScienceDirect

Chemical Engineering Journal

journal homepage: www.elsevier.com/locate/cej

Bioinspired TriPhase Interfacial Design Promotes Mass Transfer for Enhanced Photocatalytic Nitrogen Fixation

Mingzhi Zhu [a], Lei Dong [a], Yiheng Wei [a], Bin Xue [a], Xiuyan Wang [a,b,*], Tianmeng Zhang [a], Yanfeng Liu [a], Kai Wu [a], Guibin Li [c], Han Zuilhof [d,e,**], Hao Lu [a,b,*]

[a] College of Materials and Textile Engineering, Jiaxing University, Jiaxing, Zhejiang, 314001, China
[b] G60 STI Valley Industry & Innovation Institute, Jiaxing University, Jiaxing, Zhejiang, 314001, China
[c] College of Mechanical Engineering, Jiaxing University, Jiaxing, 314001, China.
[d] College of Biological and Chemical Engineering, Jiaxing University, Jiaxing, 314001, China
[e] Laboratory of Organic Chemistry, Wageningen University, 6708 WE, Wageningen, the Netherlands

ARTICLE INFO

Keywords:
Photocatalytic nitrogen fixation
Air-water interface
g-C_3N_4/Bi_2MoO_6 heterojunction
Triphase interface
Mass transfer

ABSTRACT

Photocatalytic Nitrogen Reduction Reaction (PNRR) offers a sustainable alternative to the energy-intensive Haber-Bosch process, yet its efficiency is often constrained by sluggish mass transfer of nitrogen and water. Herein, we report a novel gas-liquid interfacial photocatalytic system composed of 3D printing clay network (CN) and its supported g-C_3N_4/Bi_2MoO_6 heterojunction, which largely overcomes current limitation of mass transfer. The engineered 3D network offers a high surface area for efficient catalyst loading, facilitates repeated internal light scattering and enhances photon harvesting. By positioning the photocatalyst at the air-water interface, the interaction of light with the active sites is no longer constrained by water depth or volume, thereby significantly improving light utilization efficiency. As a result, the CN@g-C_3N_4/Bi_2MoO_6 system achieves a remarkable ammonia production rate of 69.7 μmol·g_{cat}^{-1} h^{-1}, representing a 4.4-fold enhancement over conventional powder-based systems. This study not only strongly advances the performance of PNRR, but also provides a universal strategy for enhancing reduction of carbon dioxide through interfacial and structural engineering.

1. Introduction

Ammonia (NH_3) is an important raw material for both industrial and agricultural applications, with a substantially increasing demand each year [1,2]. Besides, NH_3 serves as an ideal hydrogen carrier due to its ability to liquefy easily for storage and transportation [3], with evident relevance for any use of hydrogen energy conversion. In industry, the Haber-Bosch process remains the main method for large-scale ammonia production, which relies on high-pressure and high-temperature conditions to facilitate the direct reaction of nitrogen (N_2) and hydrogen (H_2) over ruthenium- or iron-based catalysts [4–6]. As a result, this process requires significant energy input and capital investments, primarily due to the difficulty of breaking the strong N≡N bond in N_2. Taken together, it is becoming increasingly clear that developing a more energy-efficient and sustainable alternative for NH_3 synthesis is of critical importance [7–10].

Photocatalysis has gained significant attention for its environmental friendliness, since it is driven by the abundant and renewable energy of sunlight [11]. To improve the efficiency of photocatalytic nitrogen reduction reaction (PNRR), extensive research efforts have been made [12]. However, most currently available photocatalysts still face critical challenges, including poor N_2 adsorption and activation, as well as a limited number of reactive sites, which result in a low catalytic efficiency [13]. The construction of heterojunctions offers a promising strategy by generating a built-in electric field that promotes efficient charge separation between different semiconductors [14]. Additionally, PNRR ideally operates within a triphase (solid-liquid-gas) reaction system, where reactant mass transfer and product desorption play a crucial role in determining the overall reaction efficiency [15,16]. In conventional diphase systems, N_2 needs to be solubilized and - as a gaseous reactant - exhibits an extremely low solubility and a slow diffusion rate in water, thereby significantly limiting reaction performance. Optimizing the N_2 mass transfer is therefore essential for enhancing nitrogen fixation efficiency. In this context, constructing a tri-phase interface

* Corresponding authors at: College of Materials and Textile Engineering, Jiaxing University, Jiaxing, Zhejiang, 314001, China.
** Correspondence to: H. Zuilhof, College of Biological and Chemical Engineering, Jiaxing University, Jiaxing, 314001, China.
E-mail addresses: xiuywang@zjxu.edu.cn (X. Wang), han.zuilhof@wur.nl (H. Zuilhof), lu@zjxu.edu.cn (H. Lu).

https://doi.org/10.1016/j.cej.2025.171028
Received 23 June 2025; Received in revised form 21 October 2025; Accepted 17 November 2025
Available online 19 November 2025

provides an effective solution, allowing N_2 to reach active sites directly from the gas phase. Notably, the diffusion rate of N_2 in the gas phase is four orders of magnitude higher than in the liquid phase, making this approach highly advantageous for improving the reaction kinetics [17–20].

In nature, the photosynthesis in aquatic plants requires the simultaneous uptake of water and carbon dioxide [21,22]. To meet this dual requirement, aquatic plants utilize a specialized vascular bundle structure that transports water from the roots to the leaves through transpiration. The leaves, exposed to the air, are well-positioned to efficiently absorb carbon dioxide from the atmosphere. This natural design operating at the air-water interface elegantly addresses the challenge of delivering both water and CO_2 to the sites of photosynthesis.

Inspired by this biological mechanism, we set out to construct a reactor with a structure mimicking the structure and function of plant vascular bundles. 3D printing, known for its excellent shape replication and customizable material options, has become a valuable tool in bionic design [10,23–26]. In our work, we selected pottery clay as the printing material due to several favorable properties. Upon sintering at 900 °C, many clays acquire a strong hydrophilicity, similar to red bricks, which enables efficient water transport through capillary action, akin to plant transpiration. Leveraging this property, we fabricated a grid substrate with a vascular-bundle-inspired architecture via 3D printing.

Importantly, when the printed substrate is positioned at the air-water interface, it continuously draws water upward from the bulk liquid underneath and forms a reultrathin water film on its surface. Simultaneously, the upper part of the substrate remains exposed to a gas-phase environment rich in N_2, which can readily diffuse through the ultrathin water film. This biomimetic configuration thus strongly facilitates the co-delivery of both H_2O and N_2 to the catalytic sites, and minimizes mass transfer limitations. Unlike traditional powdered photocatalytic systems, where light must traverse a thick aqueous layer to reach the catalyst, our interfacial reactor design minimizes light attenuation. Since the catalyst is covered only by a thin water film, incident light can efficiently reach and activate the photocatalyst, thereby significantly improving photonic efficiency. Employing g-C_3N_4/Bi_2MoO_6 as a model heterojunction photocatalyst and integrating it into the biomimetic reactor, we systematically investigate enhanced PNRR operating at the ubiquitous air-water interface.

2. Experimental

2.1. Materials

Bismuth nitrate pentahydrate ($Bi(NO_3)_3$•$5H_2O$, A.R., Macklin Chemistry Co., Ltd.), sodium molybdate dihydrate (Na_2MoO_4•$2H_2O$, A.R., Aladdin Chemistry Co., Ltd.), urea (CH_4N_2O, A.R., Macklin Chemistry Co., Ltd.), ethylene glycol ($C_2H_6O_2$, A.R., Macklin Chemistry Co., Ltd.), potassium sodium tartrate tetrahydrate ($C_4H_4O_6KNa$•$4H_2O$, A.R., Aladdin Chemistry Co., Ltd.), nitrogen ($N_2 \geq 99.999$ %), Nessler's reagent (A.R., Macklin Chemistry Co., Ltd.), Nafion™ perfluorinated resin solution (Nafion™, A.R., Aladdin Chemistry Co., Ltd.), expanded polyethylene (EPE) was acquired from a retail outlet and ultrasonically cleaned with ethanol and deionized water before use. All solutions were prepared with deionized water (DI water) (resistance >18 MΩ·cm^{-1}).

2.2. Preparation of clay network (CN) substrate

The slurry ink was formed by adding 12 g of clay powder and 0.3 g of hydroxypropyl methyl cellulose into 10 mL of deionized water, under hydrothermal heating at 80 °C. The cooled slurry was printed into the desired grid structure by 3D printing (Fig. S1) and then dried at 60 °C for 24 h. Subsequently, the grid structure was heated in muffle furnace at a heating rate of 7.5 °C/min to 900 °C and maintained at this temperature for 4 h to achieve the desired clay network (CN) substrate.

2.3. Preparation of CN@g-C_3N_4/Bi_2MoO_6

To obtain CN@g-C_3N_4/Bi_2MoO_6 we adopted the synthesis method described in references [4,27], the CN substrate was firstly soaked in a solution of saturated urea for 24 h. Subsequently, the CN substrate was heated together with 12 g of urea particles in a muffle furnace, at a heating rate of 4.2 °C/min to 550 °C and then maintained at 550 °C for 4 h. After cooling to room temperature, the substrate was filtered and washed with deionized water and ethanol for three times, and the synthesis of CN@g-C_3N_4 was completed after drying. The final heterojunction was constructed by growing Bi_2MoO_6 in-situ on CN@g-C_3N_4 using a hydrothermal method. Specifically, 3.88 g of $Bi(NO_3)_3$•$5H_2O$ (8 mmol) was added into a mixed solution containing 40 mL of ethylene glycol and 10 mL of ethanol. After all components were completely dissolved, the CN@g-C_3N_4 described above was immersed in this solution for 24 h at room temperature. Subsequently, 0.484 g of Na_2MoO_4•$2H_2O$ (4 mmol) was added, stirred until fully dissolved, after which the mixture was transferred to a Teflon-lined autoclave and heated at 190 °C for 2 h. After that, the substrate was taken out, washed several times with ethanol and deionized water, and dried at 60 °C, leading finally to the CN@g-C_3N_4/Bi_2MoO_6.

2.4. Characterization

Scanning electron microscopy (SEM) images of the synthesized samples were collected on an Apreo S HiVac, em-30 COXEM korea scanning electron microscope. EPAX APEX EDS was applied for elemental analyses. X-ray diffraction (XRD) images were collected a Rigaku X-ray diffractometer (D/max rA) with Cu Kα radiation at a wavelength of 1.542 Å, and the data were collected from 10° to 80°. XPS data were obtained using a ThermoScientific Escalab 250Xi. UV–Vis absorption spectra were collected on a SHIMADZU UV-3600IPLUS spectrophotometer (200–800 nm). Photoluminescence (PL) spectra were obtained using an Edinburgh Instruments FS5 Spectrofluorometer. Electron Paramagnetic Resonance (EPR) spectra were measured using a Bruker A300. The photoelectrochemical tests were performed on a CHI650E electrochemical workstation in a three-electrode glassy cell. Indium Tin Oxide (ITO) glasses coated with fabricated CN@g-C_3N_4/Bi_2MoO_6 samples, a Pt sheet (2 cm^2), and an Ag/AgCl were as the working, auxiliary, and reference electrodes, respectively, while experiments were done in Na_2SO_4 (0.1 M) solution as the electrolyte. To make the working electrodes, 5 mg of catalyst powder was added to a mixture of 1 mL of ethanol and 200 μL of Nafion™ solution, and then the suspension was dispersed for 20 min by an ultrasonic batch. Finally, 100 μL of the sample was carefully dropped onto the ITO glass, and electrodes were dried at room temperature.

2.5. Nitrogen fixation performance

The PNRR reaction was conducted in a 100 mL double-walled glassy cylindrical photo reactor at ambient pressure and temperature. Milli-Q water and pure nitrogen were employed as feedstocks, without adding sacrificial reagent. To test the PNRR activity of photocatalysts, a fixed amount of photocatalysts was added into the reactor and then evacuated for 30 min to remove the dissolved air. A 300 W Xe lamp with a power density of 200 mWcm^{-2} ($\lambda > 400$ nm) was used as light source at a distance of 8 cm to the top of reactor (set-up in Fig. S2). Continuous magnetic stirring was applied during the photocatalysis process. Then, 4 mL of the supplied solution was collected every 30 min by a sterile syringe and filtered through 0.45 μm syringe filters, and the ammonia concentrations were determined using the Nesslerization method (see below for details). Trapping test were performed by introducing the corresponding trapping and quenching agents during the PNRR tests for ammonia synthesis, and the results were further confirmed by EPR measurements.

2.6. Determination of NH_3

The amount of generated NH_3 was determined using Nessler's reagent technique. Firstly, an ammonium ion standard curve was established (Fig. S3): NH_4^+ solutions with varying concentrations were prepared. Subsequently, 4 mL of the solutions resulting from our nitrogen fixation experiments were added into each test tube sequentially and uniformly mixed with 200 μL of potassium sodium tartrate aqueous solution as an ion masking agent and 300 μL of Nessler's reagent, followed by a 15-min static incubation. The absorbance of the mixed solution at 425 nm was then measured using a microplate reader. A standard curve was established based on the concentrations of NH_4^+ and the corresponding absorbance values.

3. Results and discussion

By integrating a bioinspired design with 3D printing technology, clay-based biomimetic microreactors were fabricated through a multistep process (Fig. 1). Firstly, a plant-inspired vascular microstructure was constructed via extrusion-based 3D printing using a clay ink. Key printing parameters, including nozzle diameter (0.6 mm), printing speed (10 $mm{\cdot}s^{-1}$), and layer height (0.55 mm), were optimized to ensure high-resolution pattern fidelity and structural continuity. Following the printing step, the grid body was subjected to a sintering process at 900 °C to remove organic binders and consolidate the ceramic framework, thereby providing the required mechanical stability and porosity for subsequent catalyst deposition. The resulting 3D-printed substrate features an interconnected porous network that mimics the hierarchical vascular channels found in plant tissues, enabling efficient simultaneous transport of both gaseous and liquid reactants. This bioinspired structural design greatly facilitates mass transfer within the microreactor, particularly under triphase reaction conditions. Subsequently, photocatalytic active heterojunctions g-C_3N_4/Bi_2MoO_6 were grown in situ on the internal surfaces of the sintered clay substrate via a solvothermal reaction. This direct integration of the catalyst within the three-dimensional microstructured support ensures robust interfacial contact, which is beneficial for constructing charge separation pathway and prolonging the lifetime of photogenerated carriers. In addition, the hierarchical porous architecture facilitates effective light penetration and multi-directional scattering, thereby improving light utilization within the reactor. To sum up, the synergistic combination of bioinspired structural design and spatially distributed catalytic sites significantly improves gas-liquid-solid interfacial interactions, and leads to accelerated mass transfer of N_2 and H_2O reactants to active sites by minimizing diffusion limitations.

Fig. 2 presents the morphology of CN@ g-C_3N_4/Bi_2MoO_6 from mm to nm scales. The substrate of the reactor features a grid structure, where the clay fiber is stacked at intervals of 2 mm (Fig. 2a). This unique structural design significantly facilitates the penetration of light into the interior of the reactor. The diameter of a single clay fiber is approximately 800 μm (Fig. 2b). Upon further magnification, it is revealed that the interior of the fiber consists of clay fragments and contains numerous pores (Fig. 2c). These pores are formed as a result of the complete sintering of the hydroxypropyl methylcellulose, which ensures the efficient transport of water within the clay fiber through capillary action. After the catalyst is loaded, the surface of the substrate undergoes a noticeable change. From its original relatively smooth state, it becomes rougher due to the presence of the catalyst (Fig. 2d). Under a higher magnification, it can be observed that the catalyst is composed of microspheres with a diameter of approximately 600 nm (Fig. 2e). These microspheres feature a nanoflower-like morphology composed of densely packed nanosheets. Upon light irradiation, the intricate arrangement of nanosheets induces multiple light scattering events, which markedly improve light harvesting and enhance overall light utilization efficiency. To corroborate the elemental composition and degree of dispersion of the catalyst on the surface of the reactor we obtained the corresponding energy dispersive X-ray (EDX) elemental mapping images (Fig. 2g-l). The results show that Bi, Mo, O, C, and N atoms are uniformly distributed. In addition, we employed a transmission electron microscope (TEM) to conduct a more in-depth analysis of the catalyst. The TEM image clearly identifies the (131) crystal plane of Bi_2MoO_6 (Fig. 2f).

The crystallographic structures of the sample powders were analyzed by XRD (Fig. 3a). For the pure g-C_3N_4 sample, a prominent diffraction peak at 27.2° corresponds to the (002) plane, which is associated with the interlayer stacking of conjugated aromatic systems. A weaker peak at 13.5° is attributed to the (100) plane, indicative of in-plane structural packing [28]. For the Bi_2MoO_6-loaded CN samples, the diffraction peaks of Bi_2MoO_6 match well with the standard orthorhombic phase of Bi_2MoO_6 (JCPDS No. 76–2388). The g-C_3N_4/Bi_2MoO_6 heterojunction has a peak shape similar to Bi_2MoO_6, because the peak of g-C_3N_4 is covered by the peak of Bi_2MoO_6 at 27.5°. After loading the heterojunction catalyst onto the CN substrate, additional peaks appear at 26.7°

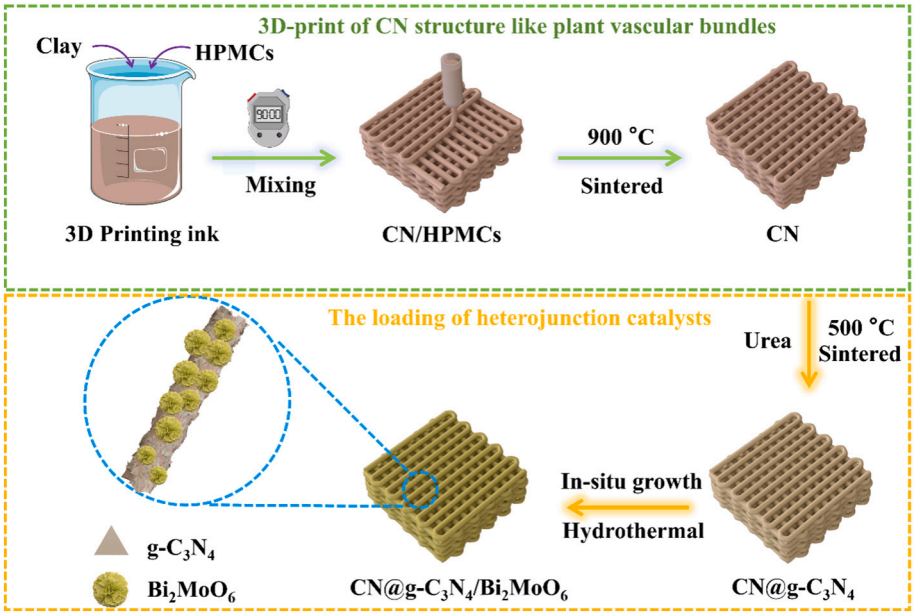

Fig. 1. Schematic diagram illustrating the preparation of CN@ g-C_3N_4/Bi_2MoO_6.

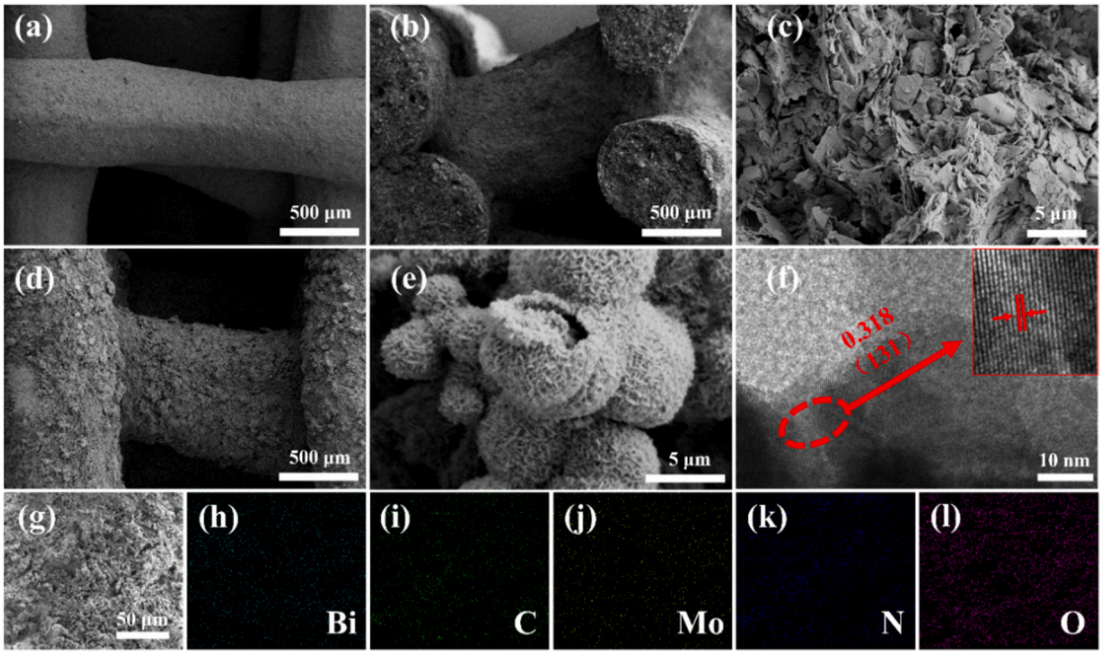

Fig. 2. SEM image of CN (a-c) and CN@g-C_3N_4/Bi_2MoO_6 (d, e); TEM images of g-C_3N_4/Bi_2MoO_6 (f) and corresponding EDX elemental mapping profiles of (h) Bi (light-blue), (i) C (green), (j) Mo (yellow), (k) N (blue), (l) O (purple) of CN@g-C_3N_4/Bi_2MoO_6.

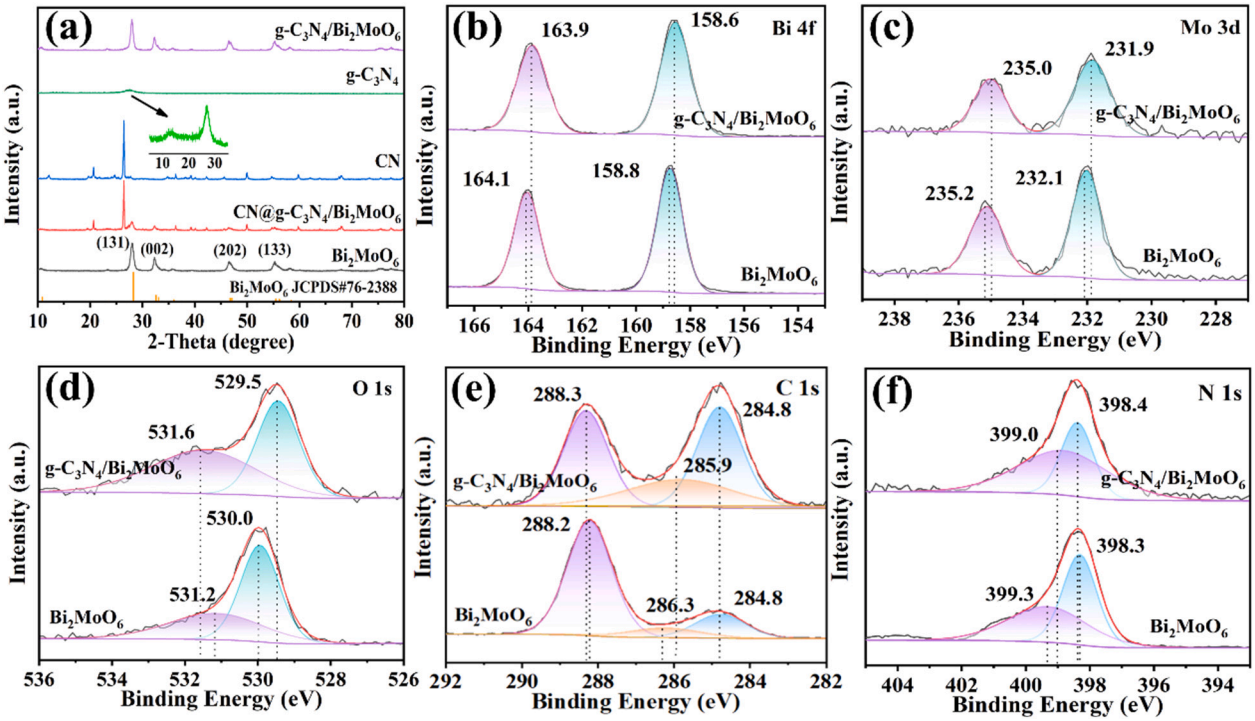

Fig. 3. (a) XRD patterns of the controlled samples; (b-d) comparative high-resolution XPS spectra between g-C_3N_4/Bi_2MoO_6 and Bi_2MoO_6, for Bi 4f (b), Mo 3d (c) and O 1s (d) core level photoelectrons; (e-f) Comparative narrow-scan XPS spectra between C_3N_4/Bi_2MoO_6 and g-C_3N_4, for C 1s (e) and N 1s (f) core level photoelectrons.

and 21.6°, which can be indexed to the (012) and (101) planes of Al_2O_3 in the clay-based (CN) substrate [3]. Notably, the characteristic peaks corresponding to the heterojunction components remain discernible, confirming their successful integration.

The chemical structure of the photocatalyst and the potential existence of any electric fields ensuing from its nanostructure was examined by XPS. The XPS spectrum confirms the presence of carbon (C 1s), nitrogen (N 1s), bismuth (Bi 4f), molybdenum (Mo 3d), and oxygen (O 1s) on the surface of the g-C_3N_4/Bi_2MoO_6 binary photocatalyst (Fig. 3b-f). The two double peaks of Bi_2MoO_6 in Fig. 3b at 164.1 and 158.8 eV correspond with the Bi $4f_{5/2}$ and Bi $4f_{7/2}$ peaks of Bi^{3+}, respectively [29]. Upon formation of the g-C_3N_4/Bi_2MoO_6 heterojunction, these peaks shift by approximately 0.2 eV toward lower binding energy. The energy shift is attributed to some electron transfer from g-C_3N_4 to Bi_2MoO_6, which increases the electron cloud density around Bi atoms, consequently reduces their binding energy, and reveals the formation of an interfacial

electric field. Similarly, the Mo 3d peaks located at 235.2 eV and 232.1 eV correspond to Mo^{6+} species [27]. A comparable shift of 0.2 eV toward lower binding energy is also observed in the Mo 3d region (Fig. 3c), further evidencing the occurrence of charge redistribution at the heterojunction interface. The O 1s spectrum (Fig. 3d) shows a broad asymmetric peak, which can be deconvoluted into two components: one centered at 531.2 eV which are attributed to combination of adsorbed oxygen species and oxygen vacancy, while another at 530.0 eV for lattice oxygen (Bi—O and Mo—O). The negative shift of the lattice oxygen peak from 530.0 eV to 529.5 eV is attributed to changes in the surface electronic environment induced by the formation of the heterojunction. Another peak at higher binding energy is assigned for combination contribution from oxygen vacancies and adsorbed oxygen species. This peak shows opposite positive shift, i.e. from 531.2 eV to 531.6 eV, the binding energy shift may be caused by an altered ratio between adsorbed oxygen and oxygen vacancies on the catalyst surface, which can reasonably occur after heterojunction construction [27]. The high-resolution C 1s spectrum (Fig. 3e) displays three distinct peaks at 288.2/288.3 eV, 286.3/285.9 eV, and 284.8 eV, corresponding, respectively, to the C═N, C-N(H), and C—C bonds, as characteristic of both pristine g-C_3N_4 and the g-C_3N_4/Bi_2MoO_6 heterojunction, respectively. The N 1s spectrum (Fig. 3f) reveals two dominant peaks: one at 398.4/398.3 eV, assigned to sp^2-hybridized nitrogen in C-N=C (C-N-C), and another at 399.0/399.3 eV, attributed to tertiary nitrogen (N-$(C)_3$) [30,31]. Overall, these XPS data thus clearly revealed the successful formation of the heterojunction and the formation of a significant electric field between the components, as was hoped for upon the initial design of the nano-heterojunction.

Next, PNRR experiments were performed at ambient temperature and pressure using visible-light irradiation ($\lambda > 400$ nm) in pure water, without the addition of any sacrificial agents. The NH_3 production was quantified colorimetrically using Nessler's reagent. To investigate the impact of the reactor configuration on the photocatalytic efficiency, three distinct reaction systems were designed: (1) a diphasic system, in which the photocatalyst is deposited on a foam base and operates fully submerged in water (Fig. 4a); and (2) a triphasic system, where the photocatalyst is positioned at the gas–liquid interface to enhance N_2 mass transfer (Fig. 4b);(3) a conventional powder suspension system (Fig. 4c).

The results show that, after constructing the heterojunction, the efficiency of g-C_3N_4/Bi_2MoO_6 reaches 16 $\mu mol \cdot g_{cat}^{-1} h^{-1}$, which represents obvious improvement compared to the two pristine catalysts g-C_3N_4 and Bi_2MoO_6 whose efficiencies are 9.5 $\mu mol \cdot g_{cat}^{-1} h^{-1}$ and 11 $\mu mol \cdot g_{cat}^{-1} h^{-1}$, respectively (Fig. 5a). Beyond that, we also tested the ammonia production performance of three (powder, diphasic, and triphasic) reaction systems above. The efficiency of the triphase reaction system has a substantial improvement as compared to the diphasic system and the powder system, reaching the value of 69.7 $\mu mol \cdot g_{cat}^{-1} h^{-1}$–4.4 times of the value for the traditional powder system (16 $\mu mol \cdot g_{cat}^{-1} h^{-1}$), and 3 times the value for the diphasic system (23.4 $\mu mol \cdot g_{cat}^{-1} h^{-1}$) (Fig. 5b). To assess the structural stability of the catalyst, XRD analysis was performed on the samples before and after the reaction (Fig. S6). The characteristic diffraction peaks of XRD pattern remained virtually unchanged, with no new peaks emerging, this confirms that the crystal structure of the catalyst was well preserved during reaction process. The superior performance of the triphasic reaction system can be attributed to its unique structural advantage, wherein portions of the catalyst are exposed to the gas phase and thus minimize any mass transfer limitations (see for more details, the discussion on Fig. 9 below). Furthermore, we investigated the correlation between catalyst loading and reactor performance. The results demonstrate that the nitrogen fixation efficiency generally increased with higher catalyst loadings, and already saturates with a loading of 1.86 % (Fig. 5c). It is noteworthy that the nitrogen fixation efficiency of our designed reactor compares favorably with other bismuth-based catalysts reported in recent years (Fig. 5d).

In order to unravel the photocatalytic mechanism of nitrogen fixation by the g-C_3N_4/Bi_2MoO_6 catalysts, in situ diffuse reflectance infrared Fourier transform spectroscopy (DRIFTS) measurements were performed. Fig. 5f shows the in situ DRIFTS spectra of the g-C_3N_4/Bi_2MoO_6 during the photocatalysis process. Series of characteristic vibrational bands can be identified, namely: peak i (1650 cm^{-1}) and peak vi (1315 cm^{-1}) assigned to the N—H stretch during the hydrogenation process; peak ii (1560 cm^{-1}) assigned to NH_3; peak iii (1543 cm^{-1}) and peak v (1450 cm^{-1}) associated with the N═N stretching vibration of the N═NH and NH=NH; peak iv (1501 cm^{-1}) assigned to the bending vibration *NH_2; and vii (1249 cm^{-1}) assigned to vibration modes of N—N of the NH_2-NH_2. The intensity of these vibrational bands increase with reaction time, the appearance and variation of these characteristic IR bands confirm an alternating hydrogenation pathway [38–41].

Control experiments further confirmed the photocatalytic origin of ammonia generation. No ammonia was detected under dark conditions, and the plain clay substrate (without either g-C_3N_4, Bi_2MoO_6, or g-C_3N_4/Bi_2MoO_6) exhibited negligible catalytic activity, indicating that the observed ammonia production arises from the light-driven catalytic activity of the g-C_3N_4/Bi_2MoO_6 composite rather than from the substrate or non-photocatalytic processes (Table S1).

To further investigate the mechanism for the enhanced PNRR activity of g-C_3N_4/Bi_2MoO_6, a detailed analysis of the electronic band structure was firstly conducted. As observed from Mott-Schottky curves, the slopes of curves g-C_3N_4 and Bi_2MoO_6 are both positive, indicating that they are both n-type semiconductors (Fig. 6a-b). The flat band potentials of g-C_3N_4 and Bi_2MoO_6 were determined to be −1.14 and −0.83 V, respectively, based on the intersection point of tangents and horizontal axis. The conduction band potential (CB) of an n-type

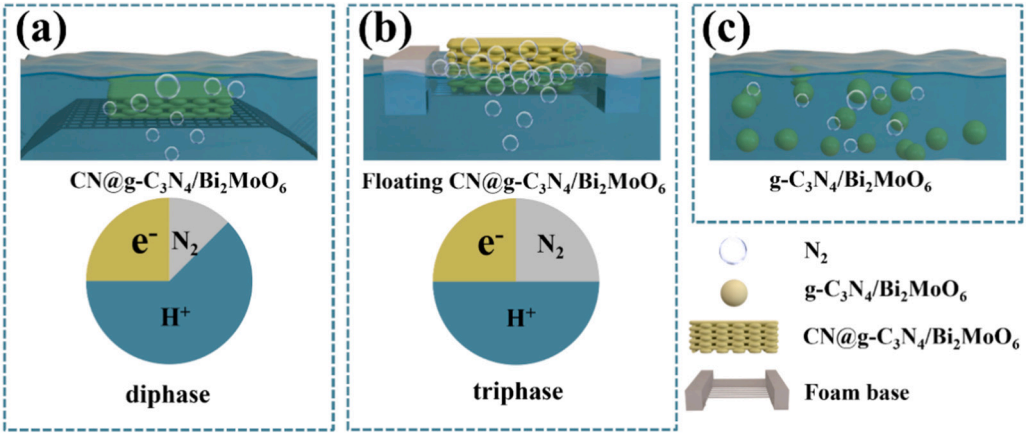

Fig. 4. Schematic structure of (a) the diphasic system, (b) the triphasic system, and (c) the traditional power reaction system.

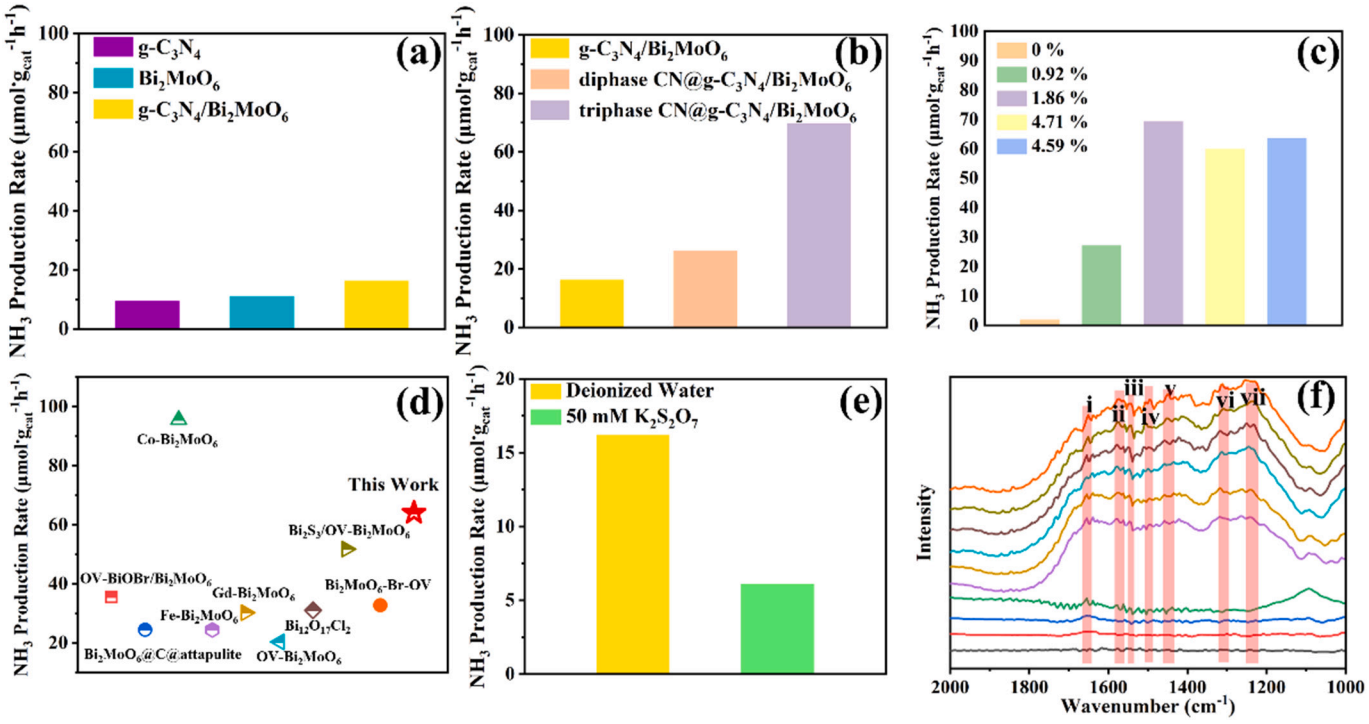

Fig. 5. (a-b) Nitrogen photofixation performance of pure g-C_3N_4, Bi_2MoO_6, the g-C_3N_4/Bi_2MoO_6 powder, the submerged biphasic system and our novel triphasic system. (c) Comparison of ammonia production efficiency of reactors with different catalyst loadings. (d) Comparison of the efficiency of bismuth-based catalysts in recent years [4,7,32–37,41,44]. (e) Electron trapping text. (f) In situ DRIFTS spectra during photothermal catalytic N_2 fixation in the presence of water vapor for g-C_3N_4/Bi_2MoO_6 system.

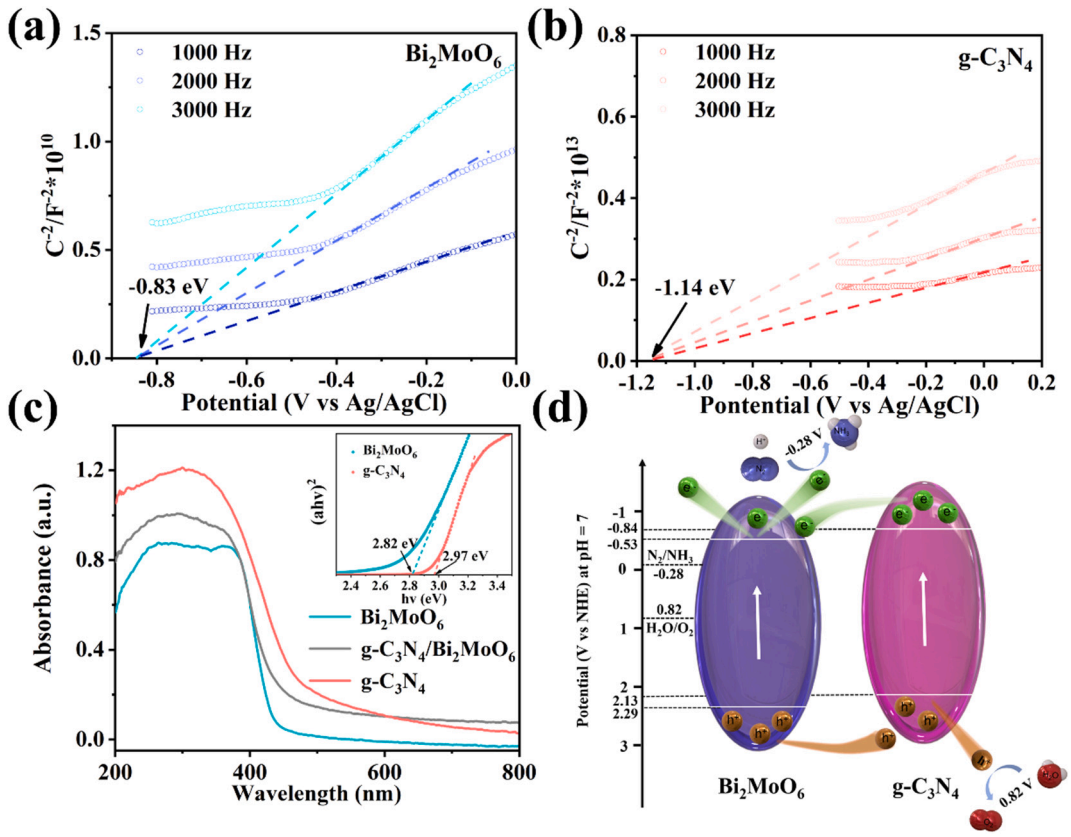

Fig. 6. Mott-Schottky plots of Bi_2MoO_6 (a) and g-C_3N_4 (b) under different alternating current potential frequency. (c) UV–Vis DRS spectra of g-C_3N_4/Bi_2MoO_6, Bi_2MoO_6 and g-C_3N_4 (the inset shows the corresponding Tauc plots [(F(*R*)hν) [2] versus photon energy (hν)]). (d) Schematic illustration of the band structure for Bi_2MoO_6 and g-C_3N_4 at pH = 7.

semiconductor is usually more positive than the flat-band potential. Thus, the CB of g-C_3N_4 and Bi_2MoO_6 were estimated to be −0.53 and −0.84 V based on experience values. In ultraviolet-visible diffuse reflectance spectroscopy (UV–Vis DRS) measurements (Fig. 6c), g-C_3N_4/Bi_2MoO_6 displayed a stronger visible-light absorption than Bi_2MoO_6, which represents a better photoresponse. Transforming the reflectance spectra to optical absorption spectra using the Kubelka-Munk equation, allowed determining from the resulting Tauc curves the electronic band gaps (E_g) of g-C_3N_4 and Bi_2MoO_6 to be 2.97 and 2.82 eV, respectively. According to the empirical formula ($E_g = E_{VB} - E_{CB}$), the valance band maximum (VB) values of g-C_3N_4 and Bi_2MoO_6 were calculated to be 2.13 and 2.29 V vs NHE, respectively [42]. The mechanism for the heterojunction enhances photocatalytic performance can be explained by Fig. 6d. The formation of the g-C_3N_4/Bi_2MoO_6 composite effects overlapping of their respective energy band structures. This leads to a reduction in the overall band gap of the heterojunction, and thus widens the light response range, and - most importantly - promotes the migration of photogenerated electrons from g-C_3N_4 to Bi_2MoO_6 with a more positive CB, while holes transfer from Bi_2MoO_6 to g-C_3N_4 with a more negative VB. This spatial separation of electrons and holes suppresses the recombination and prolongs the lifetime of carriers [43]. The holes transferred onto the g-C_3N_4 can oxidize water to produce H^+, while the now electron-rich Bi_2MoO_6 can effectively activate nitrogen and reduce nitrogen to ammonia through a hydrogenation reaction, thereby enhancing the PNRR performance.

The inherent reason for the enhanced PNRR activity by favorable heterojunction band structure was further investigated by six other techniques: photoluminescence spectroscopy (PL) and transient fluorescence, Electron Paramagnetic Resonance (EPR), photocurrent analysis, EPR spectra for g-C_3N_4/Bi_2MoO_6 and g-C_3N_4 of $\bullet O_2^-$ and •OH and molecular dynamics calculations. (1) PL spectra (Fig. 7a) show that, in contrast to pure g-C_3N_4, the composite g-C_3N_4/Bi_2MoO_6 exhibits a much lower photoluminescence, indicating a weaker recombination efficiency of photogenerated electron-hole pairs compared with g-C_3N_4. This reflects an improved charge separation and therefore the transfer of electrons to the catalyst surface for N_2 reduction. (2) The average fluorescence lifetimes of samples g-C_3N_4 and g-C_3N_4/Bi_2MoO_6 derived from fitting the transient fluorescence spectra, were calculated to be 0.75 ns and 1.76 ns, respectively. This result suggests that the construction of the heterojunction effectively enhances electron transfer, leading to a prolonged photogenerated carrier lifetime The prolonged lifetime in latter g-C_3N_4/Bi_2MoO_6 correlates with a higher charge carrier separation efficiency, which accounts for the enhanced photocatalytic performance of the heterojunction catalyst (Fig. 7b) [4]. (3) The efficiency of carrier separation and transport was considered to be a pivotal factor in the photocatalytic process. Photocurrent analysis enables a more profound insight into this procedure [10]. As displayed in Fig. 7c, the photocurrents of the g-C_3N_4/Bi_2MoO_6 composite are noticeably higher than those of the g-C_3N_4 and Bi_2MoO_6 samples. These data support that the nano-heterojunction composite improves the electron-hole separation and leads to enhanced photocurrent density. (4) Electron Paramagnetic Resonance (EPR) was employed to determine the content of oxygen vacancies. Oxygen vacancies can act as electron traps, and thus have the capacity to capture photogenerated electrons. This would create locally electron-enriched areas that facilitate the adsorption and activation of N_2 [44]. As shown in Fig. 7d, after the formation of the heterojunction, the oxygen vacancy signal of g-C_3N_4/Bi_2MoO_6 is at least three times as strong as that of the original Bi_2MoO_6. This indicates the presence of more oxygen vacancies, which likely corroborates that observed enhanced photocatalytic efficiency. (5) To further elucidate the reaction mechanism, radical trapping experiments were conducted. Firstly, we conducted electron trapping experiments using 50 mM $K_2S_2O_7$ as the electron scavenger. The results showed that the catalytic efficiency decreased from16 $\mu mol \cdot g_{cat}^{-1} h^{-1}$ to 6.1 $\mu mol \cdot g_{cat}^{-1} h^{-1}$, which we attribute to a reduction in the availability of photogenerated electrons (Fig. 5e). Additionally, the generation mechanism was investigated using EPR spectroscopy with 5,5-dimethyl-1-pyrroline N-oxide (DMPO) as a spin trapping agent. Comparative analysis of EPR spectra from the

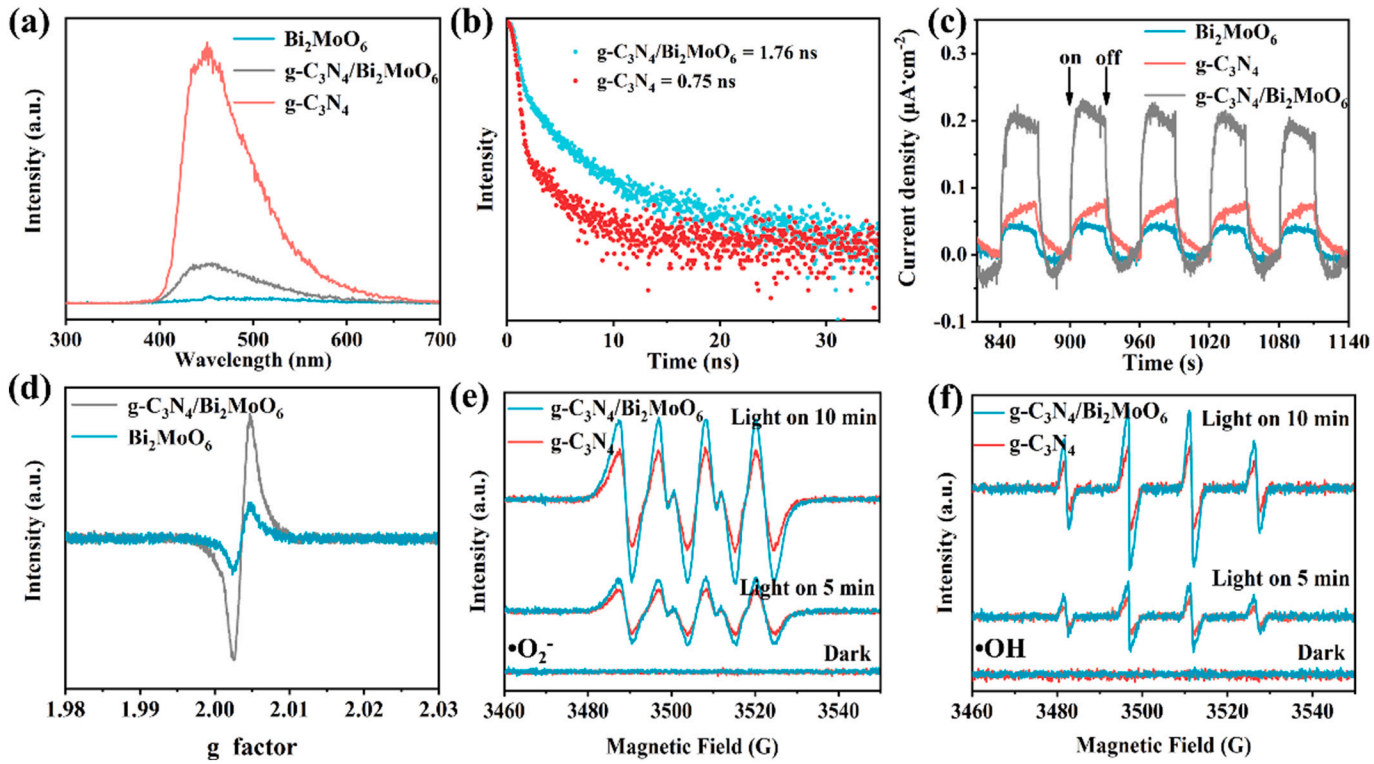

Fig. 7. (a) PL spectra for the g-C_3N_4/Bi_2MoO_6, Bi_2MoO_6 and g-C_3N_4. (b) transient fluorescence spectra of g-C_3N_4/Bi_2MoO_6 and Bi_2MoO_6. (c) Photocurrent response plots of g-C_3N_4/Bi_2MoO_6, Bi_2MoO_6 and g-C_3N_4. (d) EPR spectra of g-C_3N_4/Bi_2MoO_6 and Bi_2MoO_6. (e-f) EPR spectra for g-C_3N_4/Bi_2MoO_6 and g-C_3N_4 of $\bullet O_2^-$ and •OH (the excitation wavelength is 365 nm).

blank control and samples collected at different reaction times revealed the gradual emergence of the characteristic 1:1:1:1 quartet signal of $\bullet O_2^-$ as the reaction progressed (Fig. 7e). As the reaction time was extended from 5 to 10 min, the intensity of the 1:2:2:1 quartet signal corresponding to •OH increased significantly [29] (Fig. 7f). These results provide compelling evidence for the generation of reactive species during the reaction process. As evidenced by the consistent intensity of the EPR signals, g-C_3N_4/Bi_2MoO_6 demonstrates a superior capability to generate reactive species compared to g-C_3N_4. This enhanced generation, indicative of a greater number of active species participating in the reaction, underpins the superior efficiency of our heterojunction catalyst over its single-component counterpart.

(6) To elucidate the advantages of mass transfer within our photocatalytic device, finite element method simulation was performed by COMSOL Simulation, which is applied to study convective diffusion and mass transport of N_2 and NH_4^+ in the composite porous material region. In simulation, a single microporous channel was created (height: 100 μm, radius: 20 μm, as shown in Fig. S5a). Subsequently, a meshing process was meticulously carried out on the model. The meshed model consists a total of 14,488 domain elements, 1590 boundary elements, and 152 edge elements, which forms a well-structured computational framework for subsequent analysis (Fig. S5b). The simulation model adopts axisymmetric geometric modelling to calculate the spatial concentration distribution of N_2 and NH_4^+. In this model, the top and bottom are set as the N_2 inlet and outlet, respectively. Theoretically, the mass transfer of N_2 and NH_4^+ was mainly driven by two factors, namely the fluid flow and concentration diffusion. The governing equations are as follows:

i. $\rho(u\cdot\nabla)u = \nabla[-p + I] + K$
ii. $\rho\nabla\cdot u = 0$
iii. $\nabla\cdot Ji + u\cdot\nabla ci = Ri$
iv. $Ji = -Di\nabla c$

In the equation, the dependent variables are velocity (u), pressure (p) and concentration (ci), ρ is the fluid density, μ is the fluid viscosity, Di is the diffusion coefficient of substance i, and Ri is the reaction rate. For the mass transport simulation, the diffusion coefficients of N_2 and NH_4^+ in water are both set to 10^{-9} m^2 s^{-1}. For the 3D model of a single microporous channel, N_2 flows starting from the top, passes through the composite mesoporous material region, and flows out from the bottom. The inlet velocity was 1 cm s^{-1}. And the boundary condition at the outlet was zero pressure. The molar ratio of N_2 consumption and NH_4^+ generation was set according to $N_2 + 3\ H_2O = 2\ NH_3 + 3/2\ O_2$. In the three-phase system, the concentration of N_2 at the top inflow boundary is set to 9.6 mol m^{-3} to simulate the oxygen concentration in the atmosphere under the standard condition. The NH_4^+ concentration was set to 0 mol/m^3 for the condition mentioned above. The reaction rate constant was set to 1 mol/m^3. Simulation results in Fig. 8 illustrates that the nitrogen concentration is substantially higher in the gas phase than in the liquid phase, whereas the generated ammonium ions are primarily distributed in the liquid phase. Efficient PNRR typically requires high nitrogen accessibility, in this context, constructing a triphase interface proves to be a highly effective strategy that facilitates nitrogen transport to active sites for enhancing ammonia production.

Finally, we propose an overall summarized mechanistic illustration for photocatalytic nitrogen fixation of our triphasic CN@g-C_3N_4/Bi_2MoO_6 system in Fig. 9. Upon irradiation with visible light, the catalyst surface absorbs photons, generating electron-hole pairs. Owing to the internal electric field at the heterojunction interface, photogenerated electrons preferentially migrate to the Bi_2MoO_6 component (electron-rich domain), while holes are transferred to g-C_3N_4 (hole-rich domain), thereby achieving efficient spatial separation of charge carriers. The separated electrons drive the reduction of N_2 to NH_3, while the photogenerated holes oxidize H_2O to O_2 and H^+. The key feature of our system is the unique positioning of the catalyst at the gas-liquid-solid interface. This forms an efficient triphasic reaction environment, where nitrogen gas can directly diffuse from the atmosphere to the active catalytic sites; meanwhile, water is continuously delivered to the catalyst surface through capillary action within the hydrophilic porous clay framework. This interfacial configuration, which has clear potential for many other multicomponent photocatalytic reactions, optimizes the mass transfer of both key reactants N_2 and H_2O by significantly reducing the diffusion path length for N_2 while maintaining steady water supply, and thereby enhancing the overall reaction efficiency. Furthermore, the open 3D-printed architecture of the reactor enables direct light

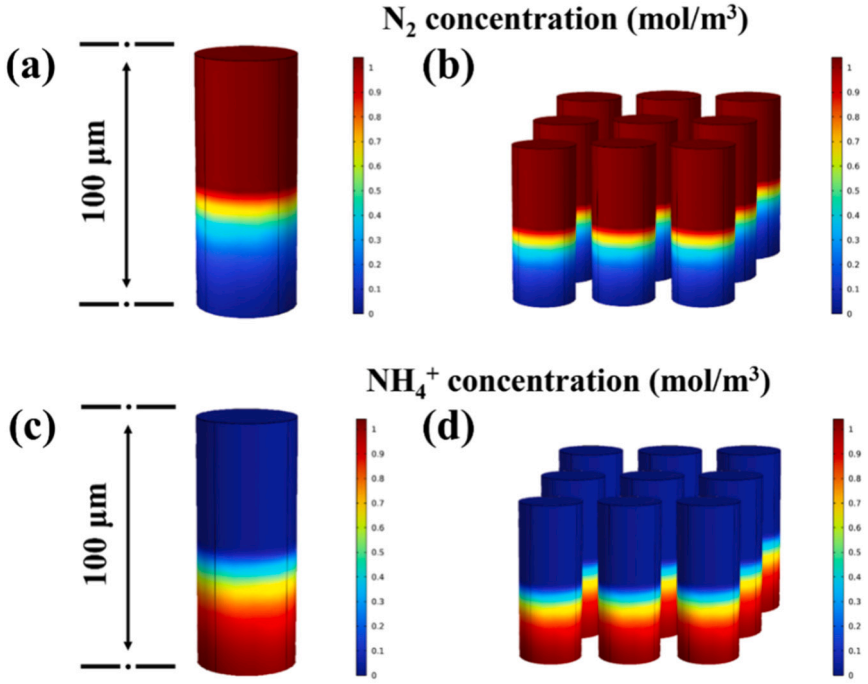

Fig. 8. Diffusion of N_2 (a-b) and NH_4^+ (c-d) in terms of concentration in a single 3D columnar structure and its 3 × 3 arrays.

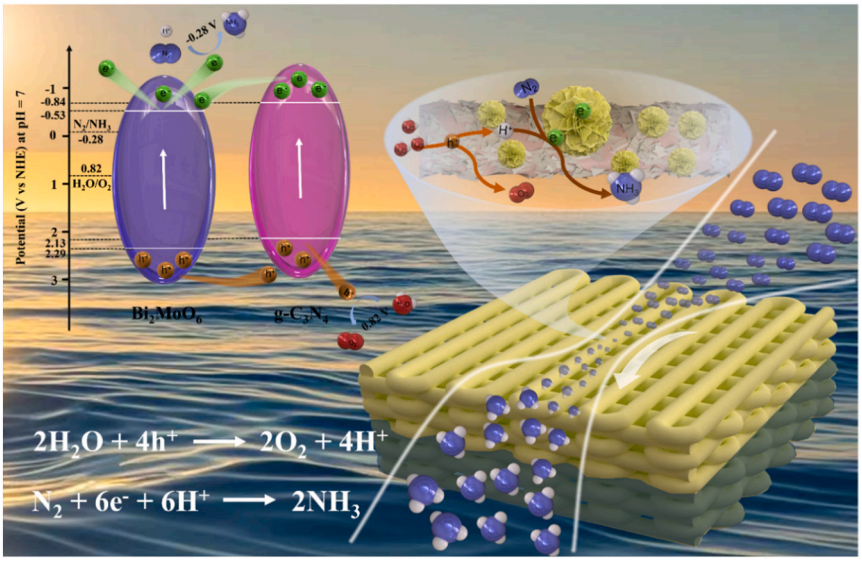

Fig. 9. Schematic illustration for the mechanism of the PNRR over CN@ g-C_3N_4/Bi_2MoO_6 under visible-light irradiation.

irradiation of the catalyst surface, while the porous network structure facilitates multiple internal light scattering events. This combination of factors effectively increases photon absorption and light utilization, resulting in a substantial boost in photocatalytic nitrogen fixation performance.

4. Conclusions

A bioinspired microreactor featuring a plant vascular bundle-mimicking structure was successfully fabricated by integrating g-C_3N_4/Bi_2MoO_6 heterojunctions as model systems onto a 3D-printed sintered clay substrate. This system operates under a triphasic photocatalytic configuration at the air-water interface, in which gas, liquid, and solid phases are spatially integrated to optimize reaction kinetics. For our model heterojunctions this triphasic system increased the overall photocatalytic conversion of N_2 to NH_3 to 69.7 $\mu mol \cdot g_{cat}^{-1}\ h^{-1}$, representing a 4.4-fold enhancement over conventional powder-based systems. From a broader viewpoint, such triphasic systems provide a novel approach for the interface engineering of other gas-involved catalytic systems that would improve significantly if mass transfer problems were reduced, such as CO_2 reduction and photocatalytic water splitting. Several of such avenues are currently being investigated in our laboratories.

CRediT authorship contribution statement

Mingzhi Zhu: Software, Methodology, Investigation. **Lei Dong:** Methodology, Investigation. **Yiheng Wei:** Methodology, Investigation. **Bin Xue:** Methodology, Investigation. **Xiuyan Wang:** Writing – review & editing, Writing – original draft, Supervision, Project administration, Methodology, Investigation, Conceptualization. **Tianmeng Zhang:** Software, Methodology, Investigation. **Yanfeng Liu:** Methodology, Investigation. **Kai Wu:** Methodology, Investigation. **Guibin Li:** Methodology, Investigation. **Han Zuilhof:** Writing – review & editing, Validation, Supervision, Funding acquisition. **Hao Lu:** Writing – review & editing, Supervision, Resources, Project administration, Funding acquisition, Conceptualization.

Declaration of competing interest

The authors declare that they have no known competing financial interests or personal relationships that could have appeared to influence the work reported in this paper.

Acknowledgement

HL and HZ acknowledge generous funding from a Top-Talent Project of Zhejiang Province (Jiaxing University). The authors would like to acknowledge the financial support from the Fundamental Research Funds for the Jiaxing University, Postgraduate Scientific Research and Practice Innovation Project of Jiaxing University (No. PSRPIP2024011B), the Research Initiation Fund Program of Jiaxing University (CD70523031) and Jiaxing University Laboratory Open Fund (No. JJ20250068), the Jiaxing Municipal Public Welfare Research Project (No. 2022AD10015). The authors gratefully acknowledge the technical contributions of Dr. Zhengping Fang with structural analysis and characterization.

Appendix A. Supplementary data

Supplementary data to this article can be found online at https://doi.org/10.1016/j.cej.2025.171028.

Data availability

Data will be made available on request.

References

[1] H. Shen, M. Yang, L. Hao, J. Wang, J. Strunk, Z. Sun, Photocatalytic nitrogen reduction to ammonia: Insights into the role of defect engineering in photocatalysts, Nano Res 15 (2022) 2773–2809, https://doi.org/10.1007/s12274-021-3725-0.
[2] X. Zhang, Y. Liu, S. Feng, X. Gu, M. Zhou, H. Wang, J. Hua, Spatial confinement of nitrogen through carboxyl-induced hydrogen bond networks in covalent organic frameworks for efficient overall ammonia photosynthesis, Appl. Catal. B Environ. 366 (2025) 125013, https://doi.org/10.1016/j.apcatb.2024.125013.
[3] X. Wang, X. Shi, S. Yin, P. She, J. Zheng, Y. Song, H. Sun, A bioinspired floatable system with a 3D sandwich-type triphase interface for highly efficient nitrogen fixation, J Mater Chem A 11 (2023) 9976–9988, https://doi.org/10.1039/d2ta08953j.
[4] C. Yang, Y. Zhang, F. Yue, R. Du, T. Ma, Y. Bian, R. Li, L. Guo, D. Wang, F. Fu, Feng, Co doping regulating electronic structure of Bi_2MoO_6 to construct dual active sites for photocatalytic nitrogen fixation, Appl. Catal. B Environ. 338 (2023) 123057, https://doi.org/10.1016/j.apcatb.2023.123057.
[5] X. Chen, L. Wu, F. Bai, NIR photothermal enhancement to achieve high-efficiency nitrogen reduction to ammonia by polyoxometalates@Fe-polydopamine, Nano Res 18 (2025) 94907006, https://doi.org/10.26599/nr.2025.94907006.
[6] S. Zhou, J. Duan, J. Shi, S. Fan, G. Chen, X. Li, Enhanced solar-driven semiconductor–Bacteria biohybrids system for N_2 reduction into ammonia, Appl. Catal. B Environ. 377 (2025) 125513, https://doi.org/10.1016/j.apcatb.2025.125513.

[7] S. Kok, W. Chong, J. Khor, R. Liu, L. Tan, J. Low, Y. Ng, X. Kong, W. Ong, S. Chai, Boosted scavenger-free overall nitrogen photofixation with molybdenum incorporated bismuth-rich oxychlorides, Small 21 (2025) 202501119, https://doi.org/10.1002/smll.202501119.

[8] S. Guo, J. Zhang, G. Fan, A. Shen, X. Wang, Y. Guo, J. Ding, C. Han, X. Gu, L. Wu, Highly efficient nitrogen reduction to ammonia through the cooperation of plasma and porous metal–organic framework reactors with confined water, Angew. Chem. Int. Ed. 63 (2024) 202409698, https://doi.org/10.1002/anie.202409698.

[9] X. Huang, R. Du, J. Ren, X. Li, M. Fu, S. Fu, T. Ma, L. Guo, R. Soomro, C. Yang, Unveiling the mechanism of aerobic photocatalytic nitrogen fixation over dynamic structural renovation on Bi_2MO_6 (M=Mo, W), ACS Catal. (2024) 13542–13549, https://doi.org/10.1021/acscatal.4c03183.

[10] R. Wu, S. Gao, C. Jones, M. Sun, M. Guo, R. Tai, S. Chen, Q. Wang, Bi/BSO heterojunctions via vacancy engineering for efficient photocatalytic nitrogen fixation, Adv. Funct. Mater. 34 (2024) 2314051, https://doi.org/10.1002/adfm.202314051.

[11] Y. Feng, L. Jiao, X. Zhuang, Y. Wang, J. Yao, The development, essence and perspective of nitrogen reduction to ammonia, Adv. Mater. 37 (2024) 202504015, https://doi.org/10.1002/adma.202410909.

[12] S. Boong, C. Carice, J. Zhang, T. Mogan, Y. Ni, H. Li, H. Lee, Single-nanoparticle-thick three-phase plasmonic catalysis for efficient nitrogen photofixation without sacrificial agents, Nano Energy 128 (2024) 109922, https://doi.org/10.1016/j.nanoen.2024.109922.

[13] L. Li, X. Lv, L. Jin, K. Du, J. Jiang, X. Zhao, H. Liang, Y. Guo, X. Wang, Facile synthesis of Sn-doped MOF-5 catalysts for efficient photocatalytic nitrogen fixation, Appl. Catal. B Environ. 344 (2024) 123586, https://doi.org/10.1016/j.apcatb.2023.123586.

[14] L. Shi, Y. Yin, S. Wang, H. Sun, Rational catalyst design for N_2 reduction under ambient conditions: strategies toward enhanced conversion efficiency, ACS Catal. 10 (2020) 6870–6899, https://doi.org/10.1021/acscatal.0c01081.

[15] Y. Liu, R. Zhou, Z. Chen, W. Tu, R. Xia, I. Emmanuel Iheanyichukwu, X. Peng, Engineering a hydrophobic–hydrophilic diphase in a Bi_2WO_6–C_3N_4 heterojunction for solar-powered CO_2 reduction, ACS Catal. (2023) 138–147, https://doi.org/10.1021/acscatal.3c03983.

[16] Y. Tang, Z. Liu, J. Jia, X. Zhong, H. Zeng, H. Xie, Z. Rui, Plasmon-assisting surface reaction on gas–vapor-solid photothermal catalytic system for efficient ammonia photosynthesis, Chem. Eng. J. 511 (2025) 161980, https://doi.org/10.1016/j.cej.2025.161980.

[17] J. Liu, R. Li, X. Zu, X. Zhang, Y. Wang, Y. Wang, C. Fan, Photocatalytic conversion of nitrogen to ammonia with water on triphase interfaces of hydrophilic-hydrophobic composite $Bi_4O_5Br_2$/ZIF-8, Chem. Eng. J. 371 (2019) 796–803, https://doi.org/10.1016/j.cej.2019.03.283.

[18] R. Shi, L. Liu, Y. Lu, C. Wang, Y. Li, L. Li, Z. Yan, J. Chen, Nitrogen-rich covalent organic frameworks with multiple carbonyls for high-performance sodium batteries, Nat. Commun. 11 (2020) 178, https://doi.org/10.1038/s41467-019-13739-5.

[19] H. Zhou, X. Sheng, J. Xiao, Z. Ding, D. Wang, X. Zhang, J. Liu, R. Wu, X. Feng, L. Jiang, Increasing the efficiency of photocatalytic reactions via surface microenvironment engineering, J. Am. Chem. Soc. 142 (2020) 2738–2743, https://doi.org/10.1021/jacs.9b12247.

[20] W. Zong, H. Gao, Y. Ouyang, K. Chu, H. Guo, L. Zhang, W. Zhang, R. Chen, Y. Dai, F. Guo, J. Zhu, Z. Zhang, C. Ye, Y.-E. Miao, J. Hofkens, F. Lai, T. Liu, Bio-inspired aerobic-hydrophobic janus interface on partially carbonized iron heterostructure promotes bifunctional nitrogen fixation, Angew. Chem. Int. Ed. 62 (2023) e202218122, https://doi.org/10.1002/anie.202218122.

[21] J. Wang, Z. Chen, L. Feng, F. Yu, C. Ran, N. Xu, Z. Jia, C. Li, Y. Zheng, W. Shi, M. Li, Plants transpiration-inspired antibacterial evaporator with multiscale structure and low vaporization enthalpy for solar steam generation, Nano Energy 114 (2023) 108631, https://doi.org/10.1016/j.nanoen.2023.108631.

[22] M. Zhou, Z. Sheng, G. Ji, X. Zhang, Aerogel-involved triple-state gels resemble natural living leaves in structure and multi-functions, Adv. Mater. 36 (2024) 2406007, https://doi.org/10.1002/adma.202406007.

[23] Q. He, T. Tang, Y. Zeng, N. Iradukunda, B. Bethers, X. Li, Y. Yang, Review on 3D printing of bioinspired structures for surface/interface applications, Adv. Funct. Mater. 34 (2023) 2309323, https://doi.org/10.1002/adfm.202309323.

[24] Y. Gao, J. Lalevée, A. Simon-Masseron, An overview on 3D printing of structured porous materials and their applications, Adv. Mater. Technol. 8 (2023) 2300377, https://doi.org/10.1002/admt.202300377.

[25] T. Li, J. Chang, Y. Zhu, C. Wu, 3D printing of bioinspired biomaterials for tissue regeneration, Adv. Healthc. Mater. 9 (2020) 2000208, https://doi.org/10.1002/adhm.202000208.

[26] Z. Feng, L. Zongan, X. Mengjia, W. Shiyan, L. Na, Y. Jiquan, A review of 3D printed porous ceramics, J. Eur. Ceram. Soc. 42 (2022) 3351–3373, https://doi.org/10.1016/j.jeurceramsoc.2022.02.039.

[27] E. Vesali-Kermani, A. Habibi-Yangjeh, H. Diarmand-Khalilabad, S. Ghosh, Nitrogen photofixation ability of g-C_3N_4 nanosheets/Bi_2MoO_6 heterojunction photocatalyst under visible-light illumination, J. Colloid Interface Sci. 563 (2020) 81–91, https://doi.org/10.1016/j.jcis.2019.12.057.

[28] Q. Meng, C. Lv, J. Sun, W. Hong, W. Xing, L. Qiang, G. Chen, X. Jin, High-efficiency Fe-mediated Bi_2MoO_6 nitrogen-fixing photocatalyst: reduced surface work function and ameliorated surface reaction, Appl. Catal. B Environ. 256 (2019) 117781, https://doi.org/10.1016/j.apcatb.2019.117781.

[29] Y. Sun, H. Wang, Q. Xing, W. Cui, J. Li, S. Wu, L. Sun, The pivotal effects of oxygen vacancy on Bi_2MoO_6: promoted visible light photocatalytic activity and reaction mechanism, Chin. J. Catal. 40 (2019) 647–655, https://doi.org/10.1016/s1872-2067(19)63277-8.

[30] P. Chen, X. Dong, M. Huang, K. Li, L. Xiao, J. Sheng, S. Chen, Y. Zhou, F. Dong, Rapid self-decomposition of g-C_3N_4 during gas–solid photocatalytic CO_2 reduction and its effects on performance assessment, ACS Catal. 12 (2022) 4560–4570, https://doi.org/10.1021/acscatal.2c00815.

[31] J. Zhao, F. Gao, S.P. Pujari, H. Zuilhof, A.V. Teplyakov, Universal calibration of computationally predicted N 1s binding energies for interpretation of XPS experimental measurements, Langmuir 33 (2017) 10792–10799, https://doi.org/10.1021/acs.langmuir.7b02301.

[32] D. Hao, J. Ren, Y. Wang, H. Arandiyan, M. Garbrecht, X. Bai, H.K. Shon, W. Wei, B.-J. Ni, A green synthesis of Ru modified g-C_3N_4 nanosheets for enhanced photocatalytic ammonia synthesis, Energy Mater. Adv. 97 (2021) 6163, https://doi.org/10.34133/2021/9761263.

[33] Q. Hao, G. Jia, W. Wei, A. Vinu, Y. Wang, H. Arandiyan, B.-J. Ni, Graphitic carbon nitride with different dimensionalities for energy and environmental applications, Nano Res 13 (2019) 18–37, https://doi.org/10.1007/s12274-019-2589-z.

[34] X. Bai, T. Jia, X. Wang, S. Hou, D. Hao, N. Bingjie, High carrier separation efficiency for a defective g-C_3N_4 with polarization effect and defect engineering: mechanism, properties and prospects, Cat. Sci. Technol. 11 (2021) 5432–5447, https://doi.org/10.1039/d1cy00595b.

[35] Y. Zhang, S. Gu, X. Zhou, K. Gao, K. Sun, D. Wu, J. Xia, X. Wang, Boosted photocatalytic nitrogen fixation by bismuth and oxygen vacancies in Bi_2MoO_6/BiOBr composite structures, Cat. Sci. Technol. 11 (2021) 4783–4792, https://doi.org/10.1039/d1cy00539a.

[36] H. Li, H. Zhao, C. Li, B. Li, B. Tao, S. Gu, G. Wang, H. Chang, Redox regulation of photocatalytic nitrogen reduction reaction by gadolinium doping in two-dimensional bismuth molybdate nanosheets, Appl. Surf. Sci. 600 (2022), https://doi.org/10.1016/j.apsusc.2022.154105.

[37] G. Wang, T. Huo, Q. Deng, F. Yu, Y. Xia, H. Li, W. Hou, Surface-layer bromine doping enhanced generation of surface oxygen vacancies in bismuth molybdate for efficient photocatalytic nitrogen fixation, Appl. Catal. B Environ. 310 (2022) 121319, https://doi.org/10.1016/j.apcatb.2022.121319.

[38] Y. Zhang, L. Guo, Y. Wang, T. Wang, T. Ma, Z. Zhang, D. Wang, B. Xu, F. Fu, In-situ anion exchange based Bi_2S_3/OV-Bi_2MoO_6 heterostructure for efficient ammonia production: a synchronized approach to strengthen NRR and OER reactions, J. Mater. Sci. Technol. 110 (2022) 152–160, https://doi.org/10.1016/j.jmst.2021.09.009.

[39] Y. Wang, Y. Zhang, Y. Gao, D. Wang, Modulating Lewis acidic active sites of Fe doped Bi_2MoO_6 nanosheets for enhanced electrochemical nitrogen fixation, J. Colloid Interface Sci. 646 (2023) 176–184, https://doi.org/10.1016/j.jcis.2023.05.012.

[40] X. Wu, F. Zhang, L. Niu, J. Liu, J. Li, D. Wang, J. Fan, X. Li, C. Shao, X. Li, Y. Liu, Promoting photocatalytic nitrogen reduction for aqueous nitrogenous fertilizer from organic wastewater over p-BiOBr/n-Bi_2MoO_6 hetero-nanofibers, Chem. Eng. J. 470 (2023), https://doi.org/10.1016/j.cej.2023.144108.

[41] P. Li, Z. Zhou, Q. Wang, M. Guo, S. Chen, J. Low, R. Long, W. Liu, P. Ding, Y. Wu, Y. Xiong, Visible-light-driven nitrogen fixation catalyzed by Bi_5O_7Br nanostructures: enhanced performance by oxygen vacancies, J. Am. Chem. Soc. 142 (2020) 12430–12439, https://doi.org/10.1021/jacs.0c05097.

[42] L. Yuan, C. Tang, P. Du, J. Li, C. Zhang, Y. Xi, Y. Bi, T. Bao, A. Du, C. Liu, Nanoporous heterojunction photocatalysts with engineered interfacial sites for efficient photocatalytic nitrogen fixation, Angew. Chem. Int. Ed. 63 (2024) e202412340, https://doi.org/10.1002/anie.202412340.

[43] T. Ma, R. Li, Y. Huang, Y. Lu, L. Guo, M. Niu, X. Huang, R. Soomro, J. Ren, Q. Wang, B. Xu, C. Yang, F. Fu, D. Wang, Interfacial chemical-bonded MoS_2/In–Bi_2MoO_6 heterostructure for enhanced photocatalytic nitrogen-to-ammonia conversion, ACS Catal. 14 (2024) 6292–6304, https://doi.org/10.1021/acscatal.3c05416.

[44] X. Xue, R. Chen, C. Yan, Y. Hu, W. Zhang, S. Yang, L. Ma, G. Zhu, Z. Jin, Efficient photocatalytic nitrogen fixation under ambient conditions enabled by the heterojunctions of n-type Bi_2MoO_6 and oxygen-vacancy-rich p-type BiOBr, Nanoscale 11 (2019) 10439–10445, https://doi.org/10.1039/c9nr02279a.